Semnan University

Progress in Physics of Applied Materials

journal homepage: https://ppam.semnan.ac.ir/

Exploring Bismuth-Induced Structural Modifications and Magnetic Phase Transitions in $CuFe_2O_4$ Ferrite

Hamid Hamrah [a], Ahmad Gholizadeh [a*]

[a] *School of Physics, Damghan University, Damghan, Iran*

ARTICLE INFO

Article history:
Received: 7 November 2024
Revised: 11 January 2025
Accepted: 11 January 2025

Keywords:
Copper Spinel Ferrite;
Copper Spinel Bismuth;
Citrate Method;
Structural Phase Transition;
Ferrimagnetic to Diamagnetic Transition.

ABSTRACT

The effects of diamagnetic bismuth substitution on the microstructural and magnetic properties of sol-gel auto-combustion citrate nitrate synthesized $CuFe_{2-x}Bi_xO_4$ (x=0.0, 0.4, 0.8, 1.2, 1.6 and 2.0) nano powders were investigated. The samples were characterized by techniques such as X-ray diffraction, Raman spectroscopy, Fourier-transform infrared spectroscopy, field-emission scanning electron microscopy, energy-dispersive X-ray spectroscopy, UV-Vis diffuse reflectance spectroscopy, and vibration sample magnetometer. The structural results showed a phase transition from a predominantly tetragonal structure with an $I4_1/amd$ space group to a tetragonal structure with a $P\bar{4}ncc$ space group. The magnetic properties of the samples revealed a transition from a ferrimagnetic to a diamagnetic phase due to the presence of the diamagnetic Bi^{3+}. Although the coercive field exhibited a minimum value at a substitution level of x = 0.8, the saturation magnetization was found to decrease with increasing Bi substitution, ranging from 25.04 emu/g for x = 0.0 to -0.02 emu/g for x = 2.0.

1. Introduction

Spinel materials are groups of mineral compounds with a general formula of AB_2X_4 that often crystallize in the cubic or tetragonal system, associated with X anions (usually halogens such as oxygen and sulfur) arranged in a close-packed cubic lattice and A and B cations occupying some or all of the octahedral and tetrahedral sites within the lattice [1-3]. A and B charges in the spinel structure are +2 and +3, respectively, with other combinations including divalent, trivalent, or tetravalent cations such as magnesium, vanadium, iron, manganese, aluminum, chromium, titanium, and silicon. Depending on the choice of anions (X), they are referred to as oxide spinels (AB_2O_4) or chalcogenide spinels (AB_2X_4, X= S, Se, Te). The natural spinel structures usually have a close-packed cubic lattice with eight tetrahedral sites and four octahedral sites in each formula unit. In oxide spinel, oxygen anions occupy the cube corners and cations occupy the tetrahedral (A) and octahedral (B) sites [4-8]. The tetrahedral sites are smaller than the octahedral sites. The B cations occupy half of the volume of the octahedral sites, while the A cations occupy one-eighth of the volume of tetrahedral sites. The inverse spinel structure has a different cation distribution, with all the A cations and half of the B cations occupying octahedral sites, while the other half of B cations occupy tetrahedral sites [8-12].

Copper ferrite is a spinel ferrimagnetic with a chemical formula $CuFe_2O_4$. A lot of studies on pure $CuFe_2O_4$ and its electrochemical and ceramic synthesis have been reported [13-18]. Moreover, $CuFe_2O_4$ is of great importance due to its high electronic conductivity, high thermal stability, and high catalytic activity. Recently, it has been shown that the significance of new applications of $CuFe_2O_4$ lies in its use as carbon-free aluminum electrolysis. The significance of this lies in the production of oxygen gas instead of CO_2 at the anode, effectively replacing the commonly used carbon. There have been extensive studies on pure $CuFe_2O_4$, and its synthesis via electrochemical and ceramic methods has

* Corresponding author. Tel.: +98-912-0816781
E-mail address: gholizadeh@du.ac.ir

Cite this article as:
Hamrah H. and Gholizadeh A., 2025. Exploring Bismuth-Induced Structural Modifications and Magnetic Phase Transitions in CuFe2O4 Ferrite. *Progress in Physics of Applied Materials, 5*(2), pp.11-21. DOI: **10.22075/PPAM.2025.35536.1120**

been reported [13]. Furthermore, $CuFe_2O_4$ is of significant importance for the completion of O_2 from the alumina-cryolite system, which is used in aluminum production, due to its high electronic conductivity, high thermal stability, and high catalytic activity. Its importance lies in its function as a non-consumable and green anode for aluminum electrolysis, where only oxygen gas is generated instead of CO_2. The distribution of cations in ferrite spinel can be represented by the following formula: $(Cu_{\delta}^{2+}Fe_{1-\delta}^{3+})_A [Cu_{1-\delta}^{2+}Fe_{1+\delta}^{3+}]_B$, where δ is the cation distribution ratio [17]. For $\delta = 1$, it shows the tetragonal phase, whereas, for $\delta = 0$, it shows the cubic phase. The tetragonal structure with space group $I4_1amd$ is stable in $CuFe_2O_4$ compositions above 663 K, while the cubic structure with space group $Fd\bar{3}m$ exhibits lower temperatures [15]. Significant research has been conducted on the synthesis of $CuFe_2O_4$ with high saturation magnetization (M_s). The $CuFe_2O_4$ is considered part of the soft ferrite group, and in addition to its common use in water purification, it is also employed in various fields such as the manufacture of electronic devices, telecommunications, remote sensing technology, microwave devices, power transmission systems, and spintronics [19, 20]. Several factors, including the synthesis method, calcination temperature, and substitutions, have been studied for their effects on the physical and magnetic properties of $CuFe_2O_4$ and other spinel ferrites. The M_s of $CuFe_2O_4$ increases with the increase of particle size, consistent with the core-shell theory, which shows that when particle sizes are small, ferrite particles have a nonmagnetic dead layer of canted surface spins on the surface [20-25]. However, a decrease leads to more canted surface spins and an increase in the dead layer which can reduce M_s.

Bismuth-based semiconductors have broad applications in catalysis, electrochemistry, and photo-catalytic processes. Among them, the $CuBi_2O_4$ spinel compound is considered a notable semiconductor due to its unique properties, including high thermal stability, water purification capability, excellent catalysis, piezoelectric and optical properties, and especially strong absorption in the visible region [26-29]. Bismuth is a semi-metal with a rhombohedral crystal structure having an anisotropic Fermi surface that makes it suitable for electronic and optical applications. The $CuBi_2O_4$ possesses intriguing characteristics, such as a p-type semiconductor behavior with high refractive index and narrow bandgap energy (1.1-2.5 eV), which make them appealing for various applications such as photovoltaic cells, sensors, optical coatings, and catalytic processes [30-35]. This material has gained attention for its potential applications in the photoelectrochemical (PEC) conversion of solar energy into chemical fuels due to its suitable band gap, p-type conductivity, and positive flat band potential. The band gap values have been determined through various experimental techniques and theoretical calculations, such as UV-VIS spectroscopy and density functional theory (DFT). However, it is important to note that the band gap of $CuBi_2O_4$ can be influenced by factors such as synthesis method, particle size, and the presence of impurities or defects in the material. Another reason for the significance of the $CuBi_2O_4$ spinel oxide is its unique structure. In this compound, Cu^{2+} and O^{2-} ions form square-planar-shaped CuO_4 units, which are connected by Bi_2O_4 chains along the c-axis. The tetragonal lattice parameters of this structure possess a c/a ratio of less than 1, where c and a represent the lattice constants along the Z and X axes, respectively. Unfortunately, its electronic properties, such as low electronic mobility and conductivity, have limited its potential for widespread use [35-36]. Consequently, numerous and diverse modifications have been explored to enhance its utility. The $CuBi_2O_4$ Nanoparticles have been synthesized through various methods, including solid-state reactions, hydrothermal processes, thermal decomposition, magnetron sputtering, microwave processing, sol-gel techniques, and more [37-39]. The development and optimization of synthesis approaches are essential for producing high-quality materials with tunable properties for specific applications.

Spinel materials with the general formula AB_2X_4 are well-known for their versatile structural and magnetic properties, making them suitable for diverse technological applications. Among them, copper ferrite ($CuFe_2O_4$) is of particular interest due to its high electronic conductivity, thermal stability, and catalytic activity. While numerous studies have focused on optimizing $CuFe_2O_4$ properties through various substitutions, the incorporation of bismuth (Bi) introduces unique advantages due to its diamagnetic nature and large ionic radius. While there may not be any specific research on the effect of bismuth substitution in place of iron on the magnetic properties of $CuFe_{2-x}Bi_xO_4$, it is important to consider studies related to bismuth substitution in other magnetic materials. This will help provide context for your research and offer insights into the potential effects of bismuth substitution on magnetic properties. Several studies have investigated the effects of bismuth substitution on the magnetic properties of various ferrite materials. For example, in cobalt ferrite ($CoFe_{2-x}Bi_xO_4$) nanoparticles, researchers observed changes in magnetic properties, such as a decrease in saturation magnetization, with increasing bismuth content [40, 41]. The hysteresis curve indicated the ferrimagnetic nature of the samples [40]. The samples also exhibited a well-saturated P-E loop with gradual lowering in remnant polarization, coercive field, and saturation polarization with an increase in bismuth concentration. Mössbauer spectroscopy analysis confirmed the changes in the magnetic moment of ions, their coupling with neighboring ions, and cation exchange interactions. The X-ray diffraction technique was used to confirm the phase purity which revealed the formation of a secondary phase when Bi^{3+} concentration exceeds $x = 0.5$ [40]. Transmission electron microscopy indicated the formation of grains by aggregation of small crystallites with a reduction in grain size to 20 nm with an increase in Bi^{3+} content [40]. Similarly, in nickel ferrite ($NiFe_{2-x}Bi_xO_4$) materials, bismuth substitution was found to alter lattice parameters and magnetic properties [42-44]. Based on magnetic studies, an increase in bismuth content leads to a decrease in the saturation magnetization, coercive field, and Néel temperature [42]. This can be attributed to the substitution of Bi^{3+} ions in the ferrite system as a nonmagnetic cation. However, the effects of Bi substitution on the structural phase transitions and magnetic properties of $CuFe_2O_4$ remain underexplored. In this study, we investigate $CuFe_{2-x}Bi_xO_4$, synthesizing nanoparticles via a sol-gel auto-

combustion method to analyze the interplay between Bi substitution and the structural and magnetic transformations. A significant novelty of this work is the identification of a phase transition from a tetragonal $I4_1/amd$ structure to a $P\bar{4}ncc$ structure, driven by Bi substitution. This structural evolution is accompanied by a ferrimagnetic-to-diamagnetic phase transition, a phenomenon not extensively studied in previous literature. Furthermore, we demonstrate that Bi substitution leads to reduced saturation magnetization and altered magnetocrystalline anisotropy, shedding light on the mechanisms driving these changes. By addressing gaps in previous research, this work paves the way for designing spinel materials with customizable properties for next-generation technologies.

2. Experimental

2.1. Materials

In this study, $CuFe_{2-x}Bi_xO_4$ (x=0.0, 0.2, 0.4, 0.6, 0.8, 1.2, 1.6, and 2.0) samples were synthesized using the sol-gel technique. Bismuth nitrate pentahydrate ($Bi(NO_3)_3.5H_2O$, Merck, >98%), iron nitrate nonahydrate ($Fe(NO_3)_3.9H_2O$, Merck, >98%), copper nitrate hexahydrate ($Cu(NO_3)_2.6H_2O$), Merck, >98%), and citric acid ($C_7O_8H_6$, Merck, >98%) were used as precursors.

2.2. Synthesis Method

$CuFe_{2-x}Bi_xO_4$ (x=0.0, 0.4, 0.8, 1.2, 1.6, and 2.0) were prepared by the citrate-nitrate method according to Refs. [45-47]. For the synthesis of the samples, high-purity metal nitrate salts (Merck) and citric acid ($C_7O_8H_6$, as chelating agents) were used. The necessary amounts of metal nitrates ($Fe(NO_3)_3.9H_2O$, and $Cu(NO_3)_3.6H_2O$) and citric acid (at a ratio of 1:1) were separately dissolved in deionized water with the aid of a magnetic stirrer. Bismuth nitrate ($Bi(NO_3)_2.5H_2O$) was dissolved in a minimal amount of nitric acid, which was then mixed with the other solutions. Subsequently, the final solution was put on a magnetic stirrer for at least 1 h until a clear and homogeneous solution was achieved. The solution was then placed in a water bath at a temperature of approximately 80 °C until a dry gel was formed. The dried gel was put in an oven at 200°C for 10 h. To achieve the spinel structure, the obtained powders were placed in a crucible and kept at 750 °C for 2 h.

2.3. Characterization

X-ray diffraction (XRD) patterns powder samples were recorded using a Bruker AXS-D8 XRD machine equipped with a Cu-Kα source (30 kV and 35 mA) and a nickel filter. The XRD analysis was performed in the 2θ range of 10-80° with a step size of 0.05° and a wavelength of 1.5404 Å. The Raman spectra of the samples were obtained using a confocal Raman spectrometer from Horiba, which utilized a laser with a wavelength of 785 nm. Field emission scanning electron microscope (FESEM) images of the samples were acquired using a TESCAN MIRA3 instrument. The magnetic properties of the samples were characterized using a Vibration Sampling Magnetometer (VSM, Lake Shore model 7400).

3. Results and Discussion

3.1. Structural Properties

The XRD patterns of $CuFe_{2-x}Bi_xO_4$ (x=0.0, 0.4, 0.8, 1.2, 1.6, and 2.0) nanoparticles are shown in Fig. 1. Structural identification performed by X'Pert shows that the dominant phase for the sample with x=0.0 has a spinel tetragonal structure with space group $I4_1/amd$, which corresponds to the standard ICDD card No. 00-034-0425 [48-51]. The lattice parameters of the spinel tetragonal structure with space group $I4_1/amd$ have the values of a = 5.788 nm and c = 8.550 nm. However, the dominant phase for the samples with (x = 0.4, 0.8, 1.2, 1.6, and 2.0) exhibits a tetragonal structure with space group $P\bar{4}ncc$, which corresponds to the standard JPCDS card No. 01-080-1908 [27, 29, 52-54]. The lattice parameters of the tetragonal structure with space group $P\bar{4}ncc$ have the values of a = 5.810 nm and c = 5.840 nm. Therefore, a structural phase transition from the tetragonal space group $I4_1/amd$ to $P\bar{4}ncc$ has been observed.

It is known that the crystal structure of $CuFe_2O_4$, depending on the Cu^{2+} ion concentration and thermal operations, can be cubic or tetragonal. Cation distribution in $CuFe_2O_4$ is as follows: $(Cu_\delta^{2+}Fe_{1-\delta}^{3+})_A [Cu_{1-\delta}^{2+}Fe_{1+\delta}^{3+}]_B$, where δ is the degree of inversion. For δ = 0, a normal phase is indicated, while δ = 1 represents an inverse spinel. The body-centered tetragonal structure is associated with the space group $I4_1/amd$ for the $CuFe_2O_4$ compound and is stable at temperatures above 663 K, whereas the face-centered cubic structure is associated with the $Fd\bar{3}m$ space group and this compound is stable at lower temperatures [48-51]. It is understood that a significant number of Cu^{2+} ions occupy the octahedral sites and the cation distribution in $CuFe_2O_4$ is as follows: $(Fe^{3+})_A[Cu^{2+}Fe^{3+}]_B$. As Bi^{3+} replaces Fe^{3+}, it is expected that Bi^{3+} ions exert pressure on the existing Cu^{2+} ions in the octahedral sites, forcing Cu^{2+} ions to migrate to tetrahedral sites. It is known that the ionic radius of Cu^{2+} is larger than that of Fe^{3+}, and the ionic radius of Bi^{3+} is significantly larger than that of Cu^{2+} and Fe^{3+}. Therefore, when Bi^{3+} ions enter the octahedral sites, they naturally displace the ion with a larger ionic radius (Cu^{2+}), causing Cu^{2+} ions to shift from the octahedral site to the tetrahedral site, resulting in a decrease in the inverse parameter. As a result, the Jahn-Teller distortion that arises from the presence of Cu^{2+} ions in the octahedral site is reduced, leading to a phase transition from $I4_1/amd$ to $P\bar{4}ncc$. This phase transition is completed in the $CuFe_2O_4$ sample.

As shown in Fig. 1, in the XRD patterns of samples $x<1$, an impurity phase of CuO is observed. However, in the XRD patterns of samples x = 1.2, and 1.6, an impurity phase of $BiFeO_3$ is observed. With the increase in Bi^{3+} ion concentration, the intensity of the secondary phase of $BiFeO_3$ also increases. Since Bi^{3+} and Fe^{3+} ions have ionic radii of 1.03 and 0.645 Å, respectively, it is likely that during the low substitution process, when Bi^{3+} ions enter the spinel structure, they completely replace Cu^{2+} and Fe^{3+} ions in the octahedral sites of the spinel. However, as the substitution increases ($1.2 \leq x \leq 1.6$), some Bi^{3+} ions do not enter the spinel structure and form an impurity phase of $BiFeO_3$. Since the process of ionic replacement to a large

extent requires high energy, Bi^{3+} ions that do not fit in the spinel structure combine with oxygen and form the impurity phase of $BiFeO_3$. Also, it is evident in the XRD patterns that with the increase in Bi^{3+} concentration, the peaks tend to shift to higher diffraction angles or larger interplanar spacing. This effect is due to the larger ionic radius of Bi^{3+} compared to Fe^{3+}, which increases the unit cell volume of the tetragonal structure.

Regarding the extent of Bi^{3+} ion's participation in the $CuFe_2O_4$ structure substitution in the present work, we clarify that for Bi^{3+} substitution in the range of $0.4 \le x \le 0.8$, the ions primarily replace Fe ions in the Fe-site. However, due to the synthesis conditions, some Cu^{2+} ions lead to the formation of a more stable impurity phase of CuO instead of tetragonal $CuBi_2O_4$. In cases of higher Bi^{3+} substitution in the range of $0.4 \le x \le 0.8$, the ions predominantly substitute for Fe ions, but due to the synthesis conditions, a more stable impurity phase of $BiFeO_3$ is formed instead of tetragonal $CuBi_2O_4$. We emphasize that the observed phase transition from space group tetragonal $I4_1/amd$ to tetragonal $P\bar{4}ncc$ serves as a key indicator of Bismuth's presence within the structure. This transition observed through X-ray diffraction analysis, demonstrates the successful incorporation of bismuth during the synthesis process.

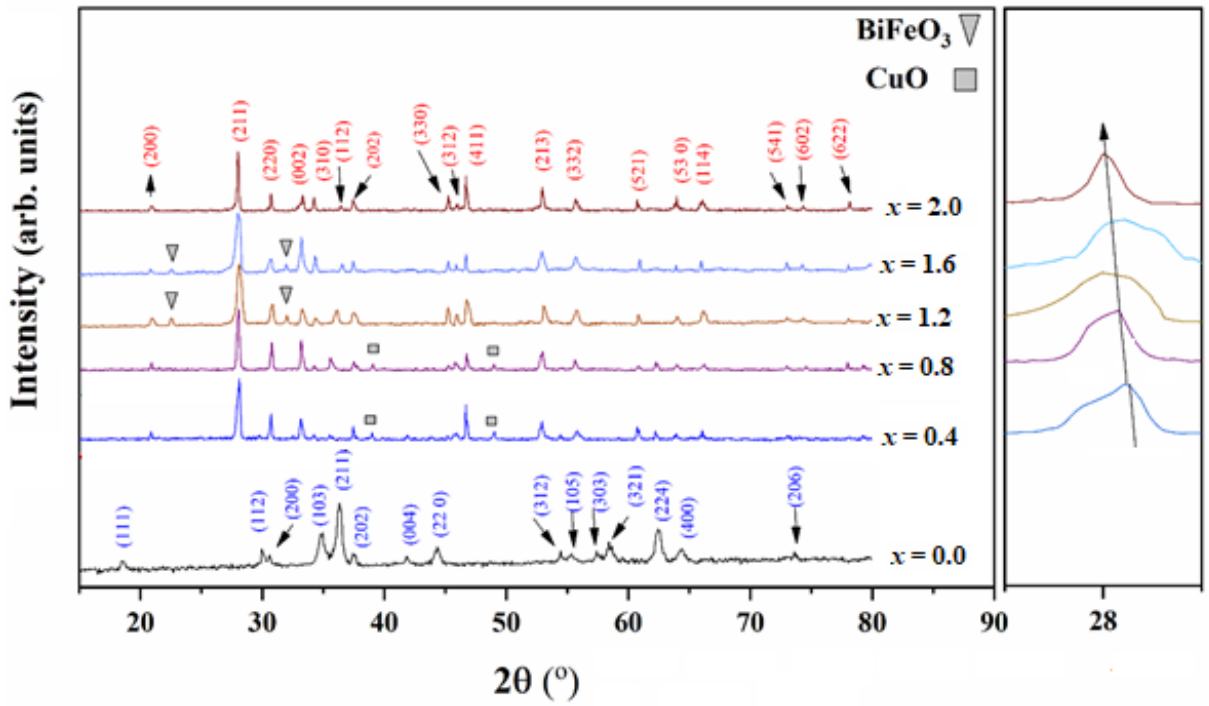

Fig. 1. XRD pattern of $CuFe_{2-x}Bi_xO_4$

3.2. Morphological Properties

The images obtained from the samples of $CuFe_{2-x}Bi_xO_4$ (x=0.0, 0.4, 0.8, 1.6, and 2.0) by field emission scanning electron microscopy at two scales of 200 nm and 1 µm are shown in Fig. 2. The effect of Bi^{3+} substitution on the morphology and particle size of the spinel can be seen from the images, as it can be observed that a set of agglomerated nanoparticles form sheet-like grains, which become larger in diameter with increasing Bi substitution, causing a decrease in sample agglomeration, which can be understood by comparing the images with a scale of 1 µm. The particle-size distribution histogram has been plotted in the inset of Fig. 2 for all samples. Using fitting of the particle size distribution with the normal-log function, the average particle size of the samples can be obtained [55, 56]:

$$P(d) = \frac{1}{d\sigma_d\sqrt{2\pi}} \exp\left(-\frac{1}{2\sigma_d^2} \ln^2\left(\frac{d}{d_{TEM}}\right)\right) \quad (1)$$

From these results, it can be inferred that the particle size has decreased with increasing Bi substitution. The decrease in particle size with increasing Bi substitution in $CuFe_{2-x}Bi_xO_4$ can be attributed to several factors related to the synthesis process and the properties of bismuth (Bi):

1. Ion size: Bismuth (Bi^{3+}) has a larger ionic radius compared to iron (Fe^{3+}), which can lead to lattice distortions when Bi substitutes for Fe in the crystal structure. These distortions may affect the nucleation and growth of the particles, potentially reducing their size.
2. Nucleation rate: The introduction of Bi may increase the nucleation rate during the synthesis process. A higher nucleation rate leads to the formation of more nuclei, which consume the available precursor materials more rapidly. This can result in a decreased particle size as each nucleus has less time to grow before the available resources are exhausted.
3. Surface energy: The presence of Bi can alter the surface energy of the particles. A higher surface energy can

make it less favorable for particles to grow, leading to smaller particle sizes.

4. Differences in reactivity: The reactivity of Bi precursors may differ from Fe precursors, which can influence particle growth kinetics during synthesis. If Bi precursors react more quickly than Fe precursors, they can limit the growth of particles, leading to smaller sizes.
5. Sintering behavior: Bismuth has a lower melting point compared to iron, which can affect the sintering behavior of the synthesized particles. The presence of Bi may lower the overall sintering temperature and reduce particle coalescence, resulting in smaller particle sizes.

These factors can contribute to the observed decrease in particle size with increasing Bi substitution in CuFe2-xBixO4. However, it's important to note that the exact mechanisms may depend on the specific synthesis conditions, such as temperature, pressure, and precursor concentrations.

EDS spectra were obtained to identify the elements forming the nanoparticles in $CuFe_{2-x}Bi_xO_4$ (x=0.0, 0.4, 0.8, 1.6, and 2.0) and are shown in Fig. 2. The peaks related to copper, iron, and oxygen elements are observed in the EDS spectrum of sample $CuFe_2O_4$, and peaks related to copper, iron, bismuth, and oxygen elements are observed in the EDS spectrum of Bi-substituted $CuFe_2O_4$, as well as peaks related to copper, bismuth, and oxygen elements are observed in the EDS spectrum of the $CuBi_2O_4$ sample, confirming the presence of these elements in the nanoparticles.

The presence of an Au peak in the EDX spectra of samples at around 2 keV can likely be attributed to the sample preparation process for analysis under a scanning electron microscope (SEM). Typically, samples are coated with a thin layer of a conductive material, such as gold or carbon, to reduce charging effects and improve the quality of the SEM images. The Au peak in the EDX spectra is therefore an artifact of the sample preparation, indicating the presence of the gold coating on the sample surface. It is essential to consider this when interpreting the EDX spectra and to ensure that the coating does not interfere with the analysis of the elements of interest.

3.3. Raman Spectra

Fig. 3 shows the Raman spectra of samples $CuFe_{2-x}Bi_xO_4$ (x=0.0, 0.4, 0.8, 1.6, and 2.0). For the $CuFe_2O_4$ sample, five vibration modes are identified, which are attributed to the single-phase $CuFe_2O_4$ structure [57]. The positions of these modes are approximately 187, 270, 475, 543, and 695 cm^{-1}, which correspond to the Raman active modes F_{2g}, E_g, F_{2g}, F_{2g}, and A_{1g} of the spinel structure, respectively. In addition, a shoulder appears around 73.74 cm^{-1}, and other weak active modes are observed at other points in the spectrum. For the $CuBi_2O_4$ sample Raman spectrum, five peaks are observed, confirming its pure phase [58]. The peak at 89.5 cm^{-1} is related to the Raman active mode B_{2g} of Bi cation on the surface. A peak at 177.85 cm^{-1} indicates the E_g vibration mode associated with the Cu-Cu bond. A peak at 288.59 cm^{-1} shows the A_{1g} bending vibration mode due to the rotation of atoms in the CuO_4 network. Another Raman peak at 438.34 cm^{-1} is attributed to the stretching vibration mode A_{1g}.

3.4. Magnetic Properties

The hysteresis loops of the $CuFe_{2-x}Bi_xO_4$ (x=0.0, 0.4, 0.8, 1.2, 1.6, and 2.0) are shown in Fig. 4. Coercive field (Hc) where the hysteresis loops cross the H-axis, remanence magnetization (Mr) where the hysteresis loops intersect the M-axis after removing the magnetic field, and Ms at the maximum magnetization point on the hysteresis loops. Since saturation is not achieved in the hysteresis loop, the law of approach to saturation (LAS) can be used to estimate the saturation magnetization (Ms) [59-62]:

$$M(H) = M_s\left[1 - \left(\frac{b}{H^2}\right) - \left(\frac{c}{H^3}\right)\right] \quad (2)$$

where $M(H)$ represents the magnetization in the presence of an external magnetic field H, and M_s signifies the saturation magnetization. Additionally, b denotes a coefficient proportional to the square of the first-order magnetocrystalline anisotropy constant K, while c is a coefficient proportional to the cube of K. This method involves extrapolating the magnetization curve to estimate M_s based on the magnetic behavior of the material at higher magnetic field strengths. The information obtained from these parameters is listed in Table 1.

Additionally, the K is obtained from the following equation [50]:

$$H_C = \frac{0.96K}{M_s} \quad (3)$$

Higher values of K indicate greater magnetic anisotropy in the material, showing that the spins strongly depend on a specific direction. According to previous report [50], there is a direct correlation between the anisotropy constant and the number of unpaired electrons, and the higher the number of unpaired electrons, the higher the value of K. The magnetocrystalline anisotropy in $CuFe_2O_4$ is due to the strong spin-orbital (L-S) coupling caused by the pairing of Cu^{2+} ions with one unpaired electron and Fe^{3+} ions with five unpaired electrons. As can be seen from Table 1, the decrease in coercivity field H_c with increasing bismuth substitution is due to the decrease in the difference of unpaired electrons between A and B cationic spins of superexchange interaction.

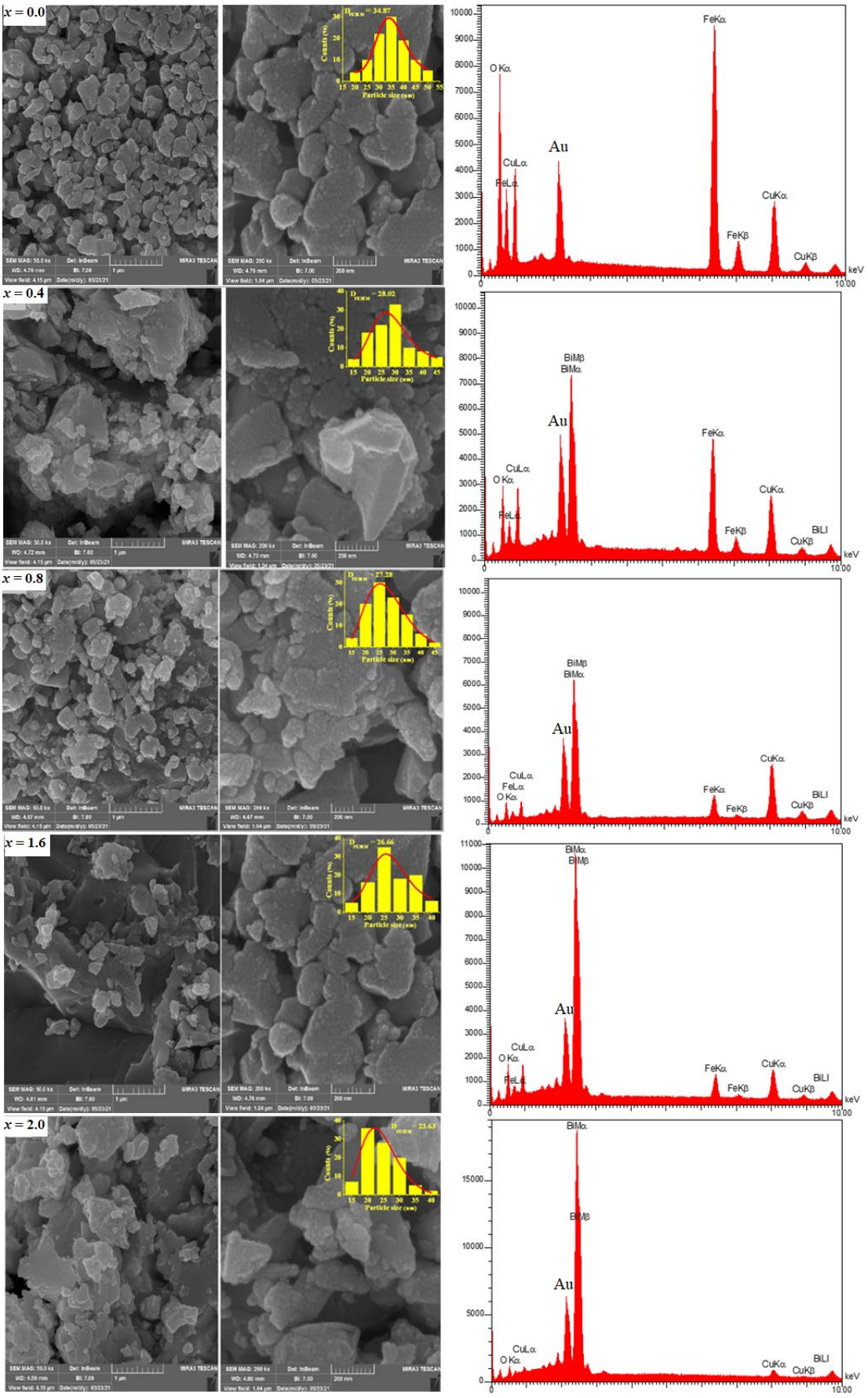

Fig. 2. FESEM images and EDS spectra of $CuFe_{2-x}Bi_xO_4$ (x=0.0, 0.4, 0.8, 1.6, and 2.0)

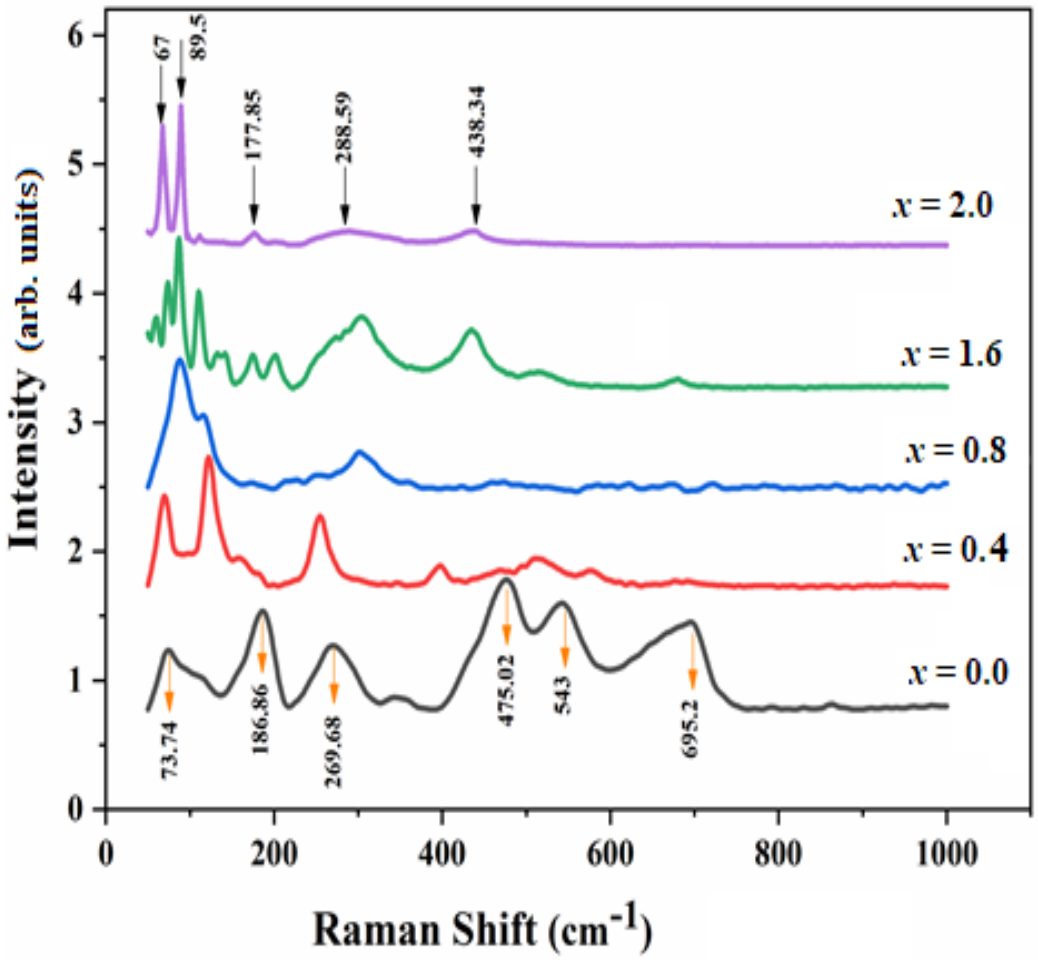

Fig. 3. Raman spectra of $CuFe_{2-x}Bi_xO_4$ (x=0.0, 0.4, 0.8, 1.6, and 2.0)

The type of anisotropy being uniaxial or cubic can be understood from the ratio M_r/M_s. If this ratio is less than 0.5, the anisotropy will be uniaxial. The calculated values of M_r/M_s for the samples in Table 1 show that the type of anisotropy is uniaxial for all samples. An increase in Bi^{3+} ions causes saturation magnetization to decrease and remanence magnetization to increase, which is attributed to the weak superexchange interaction caused by the presence of Bi^{3+} ions. This means that the Bi^{3+} ions with diamagnetic spins replace Fe^{3+} ions with 5 μ_B magnetic spins, and the total magnetization of the B sublattice decreases as a result of the total decrease in magnetization [63]. Overall, the Néel model suggests that the substitution of diamagnetic Bi^{3+} for magnetic Fe^{3+} in the octahedral site of $CuFe_4O_2$ leads to a decrease in saturation magnetization due to a combination of dilution effects, modified exchange interactions, and potential structural changes. It should be noted that Bismuth is the most important diamagnetic substance, and as can be seen from the magnetic hysteresis loop of $CuBi_2O_4$, it tilts towards negative magnetization values in high fields, demonstrating the behavior of diamagnetic material. As the substitution increases ($1.2 \leq x \leq 1.6$), some Bi^{3+} ions do not enter the spinel structure and form an impurity phase of $BiFeO_3$. The diamagnetic effect of the sample is due to the doping value of Bi. While $BiFeO_3$ is antiferromagnetic, which can reduce magnetization with further Bi substitution, it is important to note that bismuth itself is a significant diamagnetic substance. As observed in the magnetic hysteresis loop of $CuBi_2O_4$, the presence of Bi contributes to the overall magnetic behavior of the material. A remanent loop typically refers to the hysteresis loop observed in ferromagnetic materials, characterized by a non-zero magnetization at zero applied field. In our case, the diamagnetic behavior is distinct from remanence and arises from the sample's response to the highly applied magnetic field. We emphasize that the formation of a remanent loop at a lower field for sample x = 2.0 is related to measurement errors by the system. As a result, with the increase of Bi^{3+} substitution, a magnetic phase transition is observed from the ferrimagnetic phase of $CuFe_4O_2$ to the diamagnetic phase of $CuBi_2O_4$.

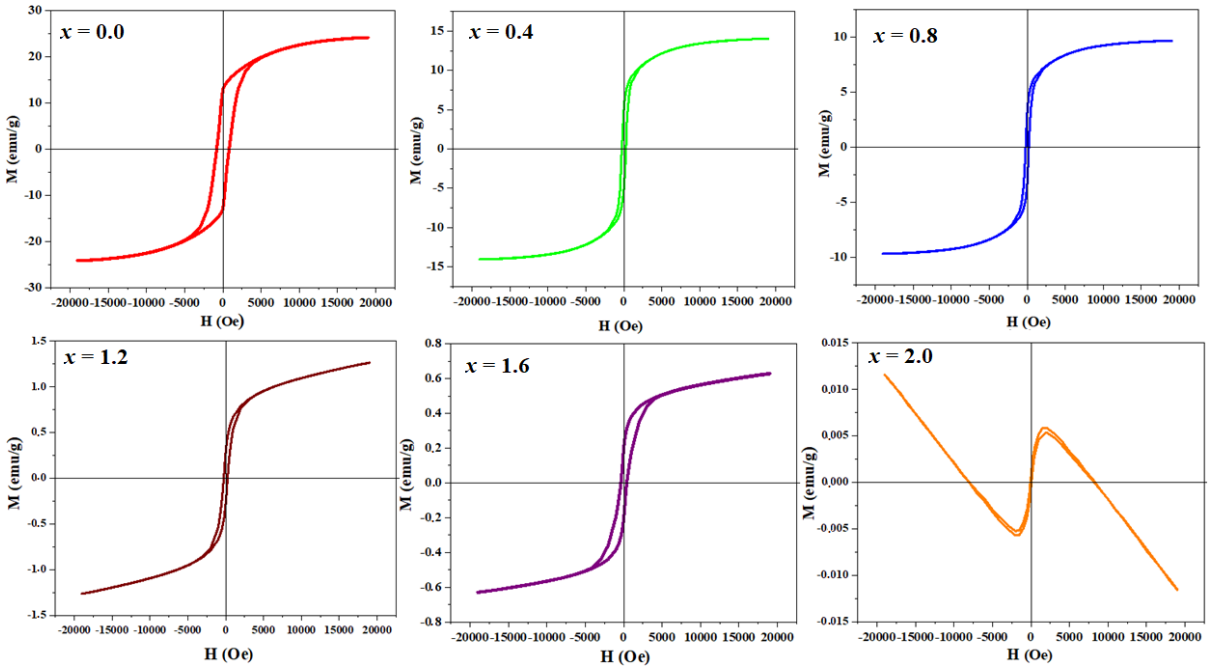

Fig. 4. Hysteresis loops of $CuFe_{2-x}Bi_xO_4$

Table 1. Values of Magnetic Parameters for $CuFe_{2-x}Bi_xO_4$ Nanoparticles

Sample	M_s(emu/g)	M_r(emu/g)	H_c(Oe)	M_r/M_s	$b*10^7$	$-c*10^{10}$	K(emu*Oe/g)
x = 0.0	25.04	13.35	815.4	0.52	1.52	5.40	21276
x = 0.4	14.33	5.19	272.1	0.35	0.94	2.93	4062
x = 0.8	9.88	3.25	209.9	0.32	0.95	2.41	2162
x = 1.2	1.33	0.28	253.4	0.20	3.70	17.76	357
x = 1.6	0.66	0.20	388.9	0.30	2.83	13.3	268
x = 2.0	-0.02	0	---	---	---	---	---

4. Conclusions

This study investigates the structural and magnetic properties of $CuFe_{2-x}Bi_xO_4$ as a function of bismuth (Bi) substitution for iron (Fe) in the octahedral site. The structural results show that the samples $CuFe_{2-x}Bi_xO_4$ exhibit a predominantly tetragonal structure with the $I4_1/amd$ space group for x = 0.0, as well as a tetragonal structure with the $P\bar{4}ncc$ space group for x = 0.4, 0.8, 1.2, 1.6, and 2.0. However, an impurity phase of CuO was observed in the samples with x = 0.0, 0.4, and 0.8, while an impurity phase of $BiFeO_3$ was found in the samples with x = 1.2, 1.6, and 2.0. Our results demonstrated a clear correlation between the degree of Bi^{3+} substitution and a decrease in saturation magnetization, with values ranging from 25.04 emu/g for x = 0 to -0.02 emu/g for x = 2.0. This reduction in the M_s can be attributed to the combined effects of dilution, altered exchange interactions, and changes in magnetocrystalline anisotropy. Additionally, the structural phase transition observed as the Bi^{3+} content increased, can contribute to the modulation of magnetic properties. These findings offer valuable insights into the complex interplay between structural transformations and magnetic phase transitions in Bi-substituted $CuFe_2O_4$ compounds, which could be useful for designing materials with tailored magnetic properties for various applications. Overall, the diverse properties of $CuFe_{2-x}Bi_xO_4$ make it a promising material for a wide range of applications in fields such as environmental remediation, sensing, energy conversion, and biomedicine.

References

[1] Rahman, M.H., Chowdhury, E.H., Redwan, D.A. and Hong, S., 2021. Computational characterization of thermal and mechanical properties of single and bilayer germanene nanoribbon. Computational Materials Science, 190, p.110272.

[2] Gholizadeh, A., 2017. A comparative study of physical properties in Fe3O4 nanoparticles prepared by coprecipitation and citrate methods. *Journal of the american ceramic society*, *100*(8), pp.3577-3588.

[3] Wang, F., Yang, H. and Zhang, Y., 2018. Enhanced photocatalytic performance of CuBi2O4 particles decorated with Ag nanowires. *Materials Science in Semiconductor Processing*, *73*, pp.58-66.

[4] Khedri, H. and Gholizadeh, A., 2019. Experimental comparison of structural, magnetic and elastic properties of M0. 3Cu0. 2Zn0. 5Fe2O4 (M= Cu, Mn, Fe, Co, Ni, Mg) nanoparticles. *Applied Physics A*, *125*(10), p.709.

[5] Stojanovic, B. ed., 2018. *Magnetic, ferroelectric, and multiferroic metal oxides*. Elsevier.

[6] Khodayari, K. and Gholizadeh, A., 2024. Exchange-spring behavior in Ni0. 3Cu0. 2Zn0. 5Fe2O4/PbFe12O19 nanocomposite. *Physica Scripta*, *99*(3), p.035932.

[7] Trompetter, B., Leveneur, J., Goddard-Winchester, M., Rumsey, B., Turner, J., Weir, G., Kennedy, J., Chong, S. and Long, N., 2023. Ferrite based soft magnetic composite development intended for inroad charging application. *Journal of Magnetism and Magnetic Materials*, *570*, p.170530.

[8] Sefatgol, R. and Gholizadeh, A., 2022. The effect of the annealing temperature on the microstructural, magnetic, and spin-dynamical properties of Mn–Mg–Cu–Zn ferrites. *Physica B: Condensed Matter*, *624*, p.413442.

[9] Huq, M.F., Saha, D.K., Ahmed, R. and Mahmood, Z.H., 2013. Ni-Cu-Zn ferrite research: a brief review. *Journal of Scientific Research*, *5*(2), pp.215-234.

[10] Beyranvand, M., Zahedi, A. and Gholizadeh, A., 2022. Cadmium substitution effect on microstructure and magnetic properties of Mg-Cu-Zn ferrites. *Frontiers in Materials*, *8*, p.779837.

[11] Liao, X., Liu, X., Wu, Y., Qian, L., Chen, Y., Wang, Y., Wu, Z., Huang, A., Liu, X. and Luo, J., 2025. Ni1-xZnxFe2O4 heterojunction composites derived from normal/inverse spinel structure for ppb-level acetone detection. *Sensors and Actuators B: Chemical*, p.137733.

[12] Shamgani, N. and Gholizadeh, A., 2019. Structural, magnetic and elastic properties of Mn0. 3− xMgxCu0. 2Zn0. 5Fe3O4 nanoparticles. *Ceramics International*, *45*(1), pp.239-246.

[13] Zhang, R., Yuan, Q., Ma, R., Liu, X., Gao, C., Liu, M., Jia, C.L. and Wang, H., 2017. Tuning conductivity and magnetism of CuFe 2 O 4 via cation redistribution. *RSC advances*, *7*(35), pp.21926-21932.

[14] Gholizadeh, A., 2018. A comparative study of the physical properties of Cu-Zn ferrites annealed under different atmospheres and temperatures: Magnetic enhancement of Cu0. 5Zn0. 5Fe2O4 nanoparticles by a reducing atmosphere. *Journal of Magnetism and Magnetic Materials*, *452*, pp.389-397.

[15] Gholizadeh, A., 2018. A comparative study of the physical properties of Cu-Zn ferrites annealed under different atmospheres and temperatures: Magnetic enhancement of Cu0. 5Zn0. 5Fe2O4 nanoparticles by a reducing atmosphere. *Journal of Magnetism and Magnetic Materials*, *452*, pp.389-397.

[16] Eghdami, F. and Gholizadeh, A., 2023. A correlation between microstructural and impedance properties of $MnFe_{2-x}Co_xO_4$ nanoparticles. Physica B: Condensed Matter, 650, p.414551.

[17] Silva, M.D.P., Silva, F.C., Sinfrônio, F.S.M., Paschoal, A.R., Silva, E.N. and Paschoal, C.W.A., 2014. The effect of cobalt substitution in crystal structure and vibrational modes of CuFe2O4 powders obtained by polymeric precursor method. *Journal of alloys and compounds*, *584*, pp.573-580.

[18] Gholizadeh, A. and Beyranvand, M., 2020. Investigation on the structural, magnetic, dielectric and impedance analysis of Mg0. 3-xBaxCu0. 2Zn0. 5Fe2O4 nanoparticles. *Physica B: Condensed Matter*, *584*, p.412079.

[19] Yadav, R.S., Kuřitka, I., Vilcakova, J., Havlica, J., Masilko, J., Kalina, L., Tkacz, J., Hajdúchová, M. and Enev, V., 2017. Structural, dielectric, electrical and magnetic properties of CuFe2O4 nanoparticles synthesized by honey mediated sol–gel combustion method and annealing effect. *Journal of Materials Science: Materials in Electronics*, *28*, pp.6245-6261.

[20] Beyranvand, M. and Gholizadeh, A., 2020. Structural, magnetic, elastic, and dielectric properties of Mn0. 3− x Cd x Cu0. 2Zn0. 5Fe2O4 nanoparticles. *Journal of Materials Science: Materials in Electronics*, *31*(7), pp.5124-5140.

[21] Hou, H., Xu, G., Tan, S. and Zhu, Y., 2017. A facile sol-gel strategy for the scalable synthesis of $CuFe_2O_4$ nanoparticles with enhanced infrared radiation property: influence of the synthesis conditions. *Infrared Physics & Technology*, *85*, pp.261-265.

[22] Gholizadeh, A. and Jafari, E., 2017. Effects of sintering atmosphere and temperature on structural and magnetic properties of Ni-Cu-Zn ferrite nano-particles: Magnetic enhancement by a reducing atmosphere. *Journal of Magnetism and Magnetic Materials*, *422*, pp.328-336.

[23] Zhang, R., Yuan, Q., Ma, R., Liu, X., Gao, C., Liu, M., Jia, C.L. and Wang, H., 2017. Tuning conductivity and magnetism of CuFe2O4 via cation redistribution. *RSC advances*, *7*(35), pp.21926-21932.

[24] Kyono, A., Gramsch, S.A., Nakamoto, Y., Sakata, M., Kato, M., Tamura, T. and Yamanaka, T., 2015. High-pressure behavior of cuprospinel CuFe2O4: Influence of the Jahn-Teller effect on the spinel structure. *American Mineralogist*, *100*(8-9), pp.1752-1761.

[25] Abharya, A. and Gholizadeh, A., 2021. Synthesis of a Fe3O4-rGO-ZnO-catalyzed photo-Fenton system with enhanced photocatalytic performance. *Ceramics International*, *47*(9), pp.12010-12019.

[26] Tahir, M.B., 2021. Construction of visible light driven CuBi2O4/Bi2WO6 solid solutions anchored with Bi12O17ClxBr2− x nanoparticles for improved photocatalytic activity. *Ceramics International*, *47*(1), pp.320-328.

[27] Soleimani, F., Salehi, M. and Gholizadeh, A., 2017. Hydrothermal synthesis, structural and catalytic studies of CuBi2O4 nanoparticles. *Journal of Nanoanalysis*, *4*(3), p.239.

[28] Li, Z., Chen, M., Zhang, Q. and Tao, D., 2020. Mechanochemical synthesis of a Z-scheme Bi2WO6/CuBi2O4 heterojunction and its visible-light photocatalytic degradation of ciprofloxacin. *Journal of Alloys and Compounds*, *845*, p.156291.

[29] Soleimani, F., Salehi, M. and Gholizadeh, A., 2019. Comparison of visible light photocatalytic degradation of different pollutants by (Zn, Mg) xCu1-xBi2O4 nanoparticles. *Ceramics International*, *45*(7), pp.8926-8939.

[30] Wang, F., Yang, H. and Zhang, Y., 2018. Enhanced photocatalytic performance of CuBi2O4 particles decorated with Ag nanowires. *Materials Science in Semiconductor Processing*, *73*, pp.58-66.

[31] Xu, J., Zhu, Y., Liu, Z., Teng, X., Gao, H., Zhao, Y. and Chen, M., 2023. Synthesis of dual Z-scheme CuBi2O4/Bi2Sn2O7/Sn3O4 photocatalysts with enhanced photocatalytic performance for the degradation of tetracycline under visible light irradiation. *Catalysts*, *13*(7), p.1028.

[32] Huang, S., Wang, G., Liu, J., Du, C. and Su, Y., 2020. A novel CuBi2O4/BiOBr direct Z-scheme photocatalyst for efficient antibiotics removal: synergy of adsorption and photocatalysis on degradation kinetics and mechanism insight. *ChemCatChem*, *12*(17), pp.4431-4445.

[33] Fu, S., Zhu, H., Huang, Q., Liu, X., Zhang, X. and Zhou, J., 2021. Construction of hierarchical CuBi2O4/Bi/BiOBr ternary heterojunction with Z-scheme mechanism for enhanced broad-spectrum photocatalytic activity. *Journal of Alloys and Compounds*, *878*, p.160372.

[34] Wu, S., Yu, X., Zhang, J., Zhang, Y., Zhu, Y. and Zhu, M., 2021. Construction of BiOCl/CuBi2O4 S-scheme heterojunction with oxygen vacancy for enhanced photocatalytic diclofenac degradation and nitric oxide removal. *Chemical Engineering Journal*, *411*, p.128555.

[35] Huang, S., Zhang, J., Qin, Y., Song, F., Du, C. and Su, Y., 2021. Direct Z-scheme SnO2/Bi2Sn2O7 photocatalyst for antibiotics removal: Insight on the enhanced photocatalytic performance and promoted charge separation mechanism. *Journal of Photochemistry and Photobiology A: Chemistry*, *404*, p.112947.

[36] Wang, R., Zhu, P., Duan, M., Xu, J., Liu, M. and Luo, D., 2021. Synthesis and characterization of successive Z-scheme CdS/Bi2MoO6/BiOBr heterojunction photocatalyst with efficient performance for antibiotic degradation. *Journal of Alloys and Compounds*, *870*, p.159385.

[37] Majhi, D., Mishra, A.K., Das, K., Bariki, R. and Mishra, B.G., 2021. Plasmonic Ag nanoparticle decorated Bi2O3/CuBi2O4 photocatalyst for expeditious degradation of 17α-ethinylestradiol and Cr (VI) reduction: Insight into electron transfer mechanism and enhanced photocatalytic activity. *Chemical Engineering Journal*, *413*, p.127506.

[38] Wang, X., Su, N., Wang, X., Cao, D., Xu, C., Wang, X., Yan, Q., Lu, C. and Zhao, H., 2024. Fabrication of 0D/1D S-scheme CoO-CuBi2O4 heterojunction for efficient photocatalytic degradation of tetracycline by activating peroxydisulfate and product risk assessment. *Journal of Colloid and Interface Science*, *661*, pp.943-956.

[39] Ma, C., Ma, D.K., Yu, W., Chen, W. and Huang, S., 2019. Ag and N-doped graphene quantum dots co-modified CuBi2O4 submicron rod photocathodes with enhanced photoelectrochemical activity. *Applied surface science*, *481*, pp.661-668.

[40] Routray, K.L., Sanyal, D. and Behera, D., 2017. Dielectric, magnetic, ferroelectric, and Mossbauer properties of bismuth substituted nanosized cobalt ferrites through glycine nitrate synthesis method. *Journal of Applied Physics*, *122*(22).

[41] Saputro, D.E. and Purnama, B., 2019, February. XRD and FTIR analysis of bismuth substituted cobalt ferrite synthesized by co-precipitation method. In *Journal of Physics: Conference Series* (Vol. 1153, No. 1, p. 012057). IOP Publishing.

[42] Jafari Fesharaki, M., Nabiyouni, G., Shahdoost, B. and Akhtarianfar, S.F., 2016. Magnetic Investigation of Various NiFe 2− x Bi x O 4 Ferrite Nanostructures Synthesized by Ball Milling Technique. Journal of Cluster Science, 27, pp.1005-1015.

[43] Praveena, K., Radhika, B. and Srinath, S., 2014. Dielectric and magnetic properties of NiFe2-xBixO4 nanoparticles at microwave frequencies prepared via co-precipitation method. *Procedia Engineering*, *76*, pp.1-7.

[44] Isfahani, M.J.N., Isfahani, P.N., Da Silva, K.L., Feldhoff, A. and Šepelák, V., 2011. Structural and magnetic properties of NiFe2− xBixO4 (x= 0, 0.1, 0.15) nanoparticles prepared via sol–gel method. *Ceramics International*, *37*(6), pp.1905-1909.

[45] Sefatgol, R., Gholizadeh, A. and Hatefi, H., 2024. Effect of Ti Substitution on the Structural, Optical, and Magnetic Properties of Mn-Mg-Cu-Zn Ferrite Prepared by the Sol–Gel Route. *Journal of Electronic Materials*, *53*(10), pp.6140-6150.

[46] Noori, F. and Gholizadeh, A., 2020. Structural, optical, magnetic properties and visible light photocatalytic activity of BiFeO3/graphene oxide nanocomposites. *Materials Research Express*, *6*(12), p.1250g1.

[47] Adineh, Z. and Gholizadeh, A., 2024. Comparison of sol–gel and hydrothermal synthesis methods on the physical, and photocatalytic properties of Bi1− x Ce x Fe1− x Al x O3 ferrites. *Journal of Materials Science: Materials in Electronics*, *35*(11), p.745.

[48] Sefatgol, R., Gholizadeh, A. and Hatefi, H., 2024. Enhancement of magnetic properties of bismuth-substituted Mn-Mg-Cu-Zn ferrite prepared by sol-gel route. *Journal of Sol-Gel Science and Technology*, pp.1-14.

[49] Mojahed, M., Dizaji, H.R. and Gholizadeh, A., 2022. Structural, magnetic, and dielectric properties of Ni/Zn co-substituted CuFe2O4 nanoparticles. *Physica B: Condensed Matter*, *646*, p.414337.

[50] Choupani, M. and Gholizadeh, A., 2024. Correlation between structural phase transition and physical properties of Co2+/Gd3+ co-substituted copper ferrite. *Journal of Rare Earths*, *42*(7), pp.1344-1353.

[51] Mojahed, M., Gholizadeh, A. and Dizaji, H.R., 2024. Influence of Ti4+ substitution on the structural, magnetic, and dielectric properties of Ni-Cu–Zn ferrite. *Journal of Materials Science: Materials in Electronics*, *35*(18), p.1239.

[52] Harish, V., Ansari, M.M., Tewari, D., Gaur, M., Yadav, A.B., García-Betancourt, M.L., Abdel-Haleem, F.M., Bechelany, M. and Barhoum, A., 2022. Nanoparticle and nanostructure synthesis and controlled growth methods. *Nanomaterials*, *12*(18), p.3226.

[53] Gao, H., Wang, F., Wang, S., Wang, X., Yi, Z. and Yang, H., 2019. Photocatalytic activity tuning in a novel Ag2S/CQDs/CuBi2O4 composite: Synthesis and photocatalytic mechanism. *Materials Research Bulletin*, *115*, pp.140-149.

[53] Gao, H., Wang, F., Wang, S., Wang, X., Yi, Z. and Yang, H., 2019. Photocatalytic activity tuning in a novel Ag2S/CQDs/CuBi2O4 composite: Synthesis and photocatalytic mechanism. *Materials Research Bulletin*, *115*, pp.140-149.

[54] Guo, F., Li, M., Ren, H., Huang, X., Hou, W., Wang, C., Shi, W. and Lu, C., 2019. Fabrication of pn CuBi2O4/MoS2 heterojunction with nanosheets-on-microrods structure for enhanced photocatalytic activity towards tetracycline degradation. *Applied Surface Science*, *491*, pp.88-94.

[55] Gholizadeh, A. and Malekzadeh, A., 2017. Structural and redox features of La0. 7Bi0. 3Mn1− xCoxO3

nanoperovskites for ethane combustion and CO oxidation. *International Journal of Applied Ceramic Technology*, *14*(3), pp.404-412.

[56] Hosseini, S. and Gholizadeh, A., 2023. Optimizing physical properties of BiFe1-xMnxO3 perovskite thin films via a low-temperature sol-gel method. *Ceramics International*, *49*(24), pp.40258-40267.

[57] Kumar, S., Kumari, K., Kumar, A., Koo, B.H. and Vij, A., 2023. Raman spectroscopy of spinel ferrites. In *Ferrite Nanostructured Magnetic Materials* (pp. 537-555). Woodhead Publishing.

[58] Shah, A.K., Sahu, T.K., Banik, A., Gogoi, D., Peela, N.R. and Qureshi, M., 2019. Reduced graphene oxide modified CuBi2O4 as an efficient and noble metal free photocathode for superior photoelectrochemical hydrogen production. *Sustainable Energy & Fuels*, *3*(6), pp.1554-1561.

[59] Faramawy, A.M. and El-Sayed, H.M., 2024. Enhancement of magnetization and optical properties of CuFe2O4/ZnFe2O4 core/shell nanostructure. *Scientific Reports*, *14*(1), p.6935.

[60] Adineh, Z. and Gholizadeh, A., 2021. Hydrothermal synthesis of Ce/Zr co-substituted BiFeO3: R 3 c-to-P 4 mm phase transition and enhanced room temperature ferromagnetism. *Journal of Materials Science: Materials in Electronics*, *32*(22), pp.26929-26943.

[61] Devi, E.C. and Singh, S.D., 2023. Law of approach to saturation magnetization with structural and temperature variation in Ni–Zn ferrites. *Physica Scripta*, *98*(5), p.055938.

[62] Kurian, J. and Mathew, M.J., 2017. A facile approach to the elucidation of magnetic parameters of CuFe2O4 nanoparticles synthesized by hydrothermal route. *Journal of Magnetism and Magnetic Materials*, *428*, pp.204-212.

[63] Spaldin, N.A., 2010. *Magnetic materials: fundamentals and applications*. Cambridge university press.